Post-irradiation microstructural characterization on 3.5-MeV self-ion irradiated ferritic/martensitic steels at a radiation damage level of 480 dpa

Myeongkyu Lee, Sangjoon Ahn*

Department of Nuclear Engineering, Ulsan National Institute of Science and Technology (UNIST)
50 UNIST-gil, Ulsan, Republic of Korea, 44919
Corresponding author:sjahn99@unist.ac.kr

1. Introduction

Ferritic/martensitic (F/M) steel alloys are one of the most promising candidates for cladding components in the harsh operating conditions of Gen IV fast reactors [1,2]. Historically, these types of steels have exhibited superb radiation resistance as well as excellent thermophysical characteristics [3]. Even with these F/M steels' superiorities, however, potential radiation-induced mechanical degradations such as creep properties in high temperature regime have instigated further research on creep-resistant ferritic/martensitic steel alloys.

FC92 is a series of Grade 92 (Gr.92)-based F/M steels, developed by the Korea Atomic Energy Research Institute (KAERI). At the out-of-pile test on thermos-physical properties, these Gr.92-modified alloys demonstrated ~30% improved creep strength at 650 °C as compared to HT9 [4]. These favorable performance of FC92 alloys make them the candidate materials for fuel cladding material in the prototype Generation-IV (Gen-IV) sodium-cooled fast reactor (PGSFR). They underwent the in-reactor irradiation utilizing the BOR-60 in Russia from 2014 to 2019 and then radiation damage achieved after 6-year irradiation in BOR-60 was estimated to reach only ~75 dpa.

Therefore, the objective of this study is to investigate the radiation response of newly-developed F/M steels at higher radiation damage conditions than 75 dpa with a comparison to two reference steels of HT9 and Gr.92. In this study, radiation damage was emulated utilizing accelerator-based ion irradiating technique; the irradiation was conducted with 3.5 MeV Fe^{++} ions at 475°C up to a peak radiation damage of 480 dpa. A post-irradiation examination was conducted with a focus on microstructural instability evolution utilizing a field-emission transmission electron microscopy (FE-TEM) and the ChemiSTEM energy-dispersive X-ray spectroscopy (EDS).

2. Experimental

2.1. Pre-irradiation sample process

As-received F/M alloy plates of HT9, Gr.92, FC92-B, and FC92-N was electrical discharge machining (EDM)-machined into cubes of which dimension was 1 mm × 1 mm × 1 mm. Each sectioned cube was heat-treated at 1,000 °C/30 min/air-cooling and then tempered 750 °C/60 min/air-cooling to room temperature. Before irradiation, the surface of heat-treated alloy specimens was flattened up to #4000 SiC papers followed by stepwise polishing process with 6, 3, 1, and 0.25 μm diamond suspensions and 0.02 μm colloidal silica suspension.

2.2. Ion irradiation

The mirror-polished steel specimens underwent two-step ion irradiation processes: i) helium pre-implantation at room temperature, ii) 3.5 MeV Fe^{++} ion irradiation at 475 °C. Raster-scanning type of helium ion beam was employed to mimic the in-reactor transmutation reaction in the fuel cladding material by utilizing a 400-kV ion accelerator in the accelerator laboratory of Texas A&M University. The contents of implanted helium ions varied from 0 appm at the surface to 480 appm at the Bragg's peak of 3.5 MeV Fe^{++} ions (1,000 nm depth from the surface) with a corresponding He/dpa ratio of 1 appm/dpa. After the helium-ion cold implantation, 3.5-MeV defocused type Fe^{++} ions were irradiated on the very same surface at 475 °C using a 1.7-MV Ionex Tandetron Accelerator. The nominal radiation damage was 480 dpa at its dpa peak at a depth of 1,000 nm from the surface. The four tested alloys were irradiated at the same time to avoid the fluctuation in dose rate and irradiating temperature.

2.3. Post-irradiation microstructure characterization

After irradiation, the irradiated alloys were focused-ion-beam (FIB)-fabricated into a thin foil of which dimension was 5 μm × 7 μm × 100 nm utilizing Helios 450 HP manufactured by FEI. More than three TEM specimens were prepared to avoid spatial inhomogeneity in cavity and secondary-phase evolution along ion path. The TEM imaging was conducted under conventional-TEM (CTEM) and scanning-TEM (STEM) mode utilizing FE-TEM (FEI Titan G2 equipped with ChemiSTEM Cs Probe). The bright field (BF) and high-angle annular dark-field (HAADF) images were simultaneously obtained at the magnifications of 14k, 57k, and 110k. A qualitative ChemiSTEM elemental analysis was performed on the radiation-damage regions to identify the radiation-induced secondary-phase evolution.

HAADF images

(a) Irradiated HT9   (b) Irradiated Gr.92   (c) Irradiated FC92-B   (d) Irradiated FC92-N

BF images

(e) Irradiated HT9   (f) Irradiated Gr.92   (g) Irradiated FC92-B   (h) Irradiated FC92-N
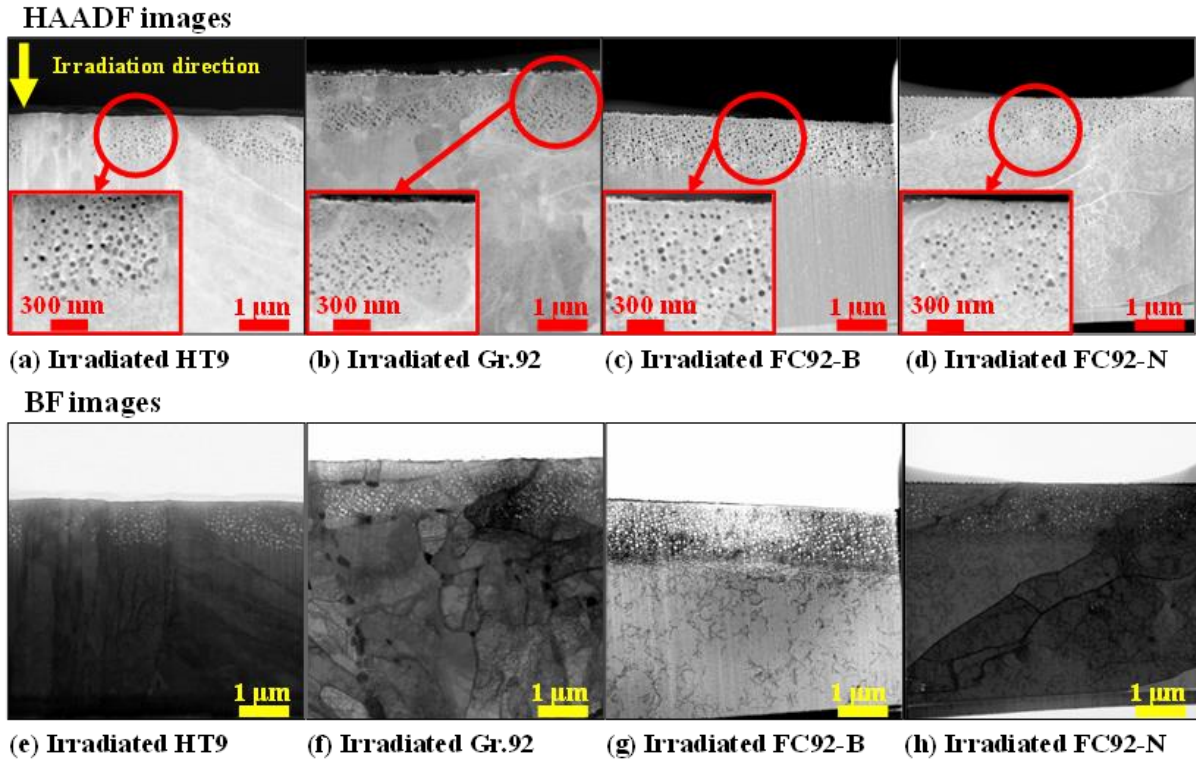
Fig. 1 Low-magnification (14k or 20k) HAADF (a-d); BF (e-h) STEM images of Fe^{++} ion-irradiated steels (radiation damage: 480 dpa) with He/dpa ratio of 1 appm/dpa. Representative portion of each irradiated alloys are enlarged (a magnification of 52 K) in red-boxed insets.

To distinguish cavities formed after irradiation from Fe-deficient defect clusters, a pair of BF and DF images were compared with each other to cross-check cavity evolution and, finally, double-checked with a comparison of elemental mapping images of Fe, Cr, and Ni. Each HAADF image was divided into 100-nm-thick bins over the ion-damaged regions to numerically characterize depth-dependent cavity evolution; each EDS analysis result was binned into 200-nm-thick images to investigate radiation-induced M_2X precipitate evolution. Swelling was calculated by following equation (r_i: the cavity radius, N: the number of cavities, A: the examined area, and t: TEM sample thickness):

$$S\,(\%) = \frac{\sum_{i=1}^{N} \frac{4}{3}\pi r_i^3}{A \times t - \sum_{i=1}^{N} \frac{4}{3}\pi r_i^3} \times 100 \qquad (1)$$

3. Results and discussion

3.1. General description of microstructural characteristics of the tested alloys before irradiation

Average grain size (ferret diameter) of each alloy is measured as 9.21 μm for HT9, ~7.49 μm for Gr.92, ~9.69 μm for FC92-B, and ~8.94 μm for FC92-N. Lath lengths varied from ~600 to 1,200 nm and lath widths from ~200 to ~700 nm for every tested alloy but FC92-B appeared to have the largest lath structures. Specifics regarding un-irradiated microstructure of the alloys are demonstrated in detail in Ref. [5].

3.2. Quantitative analysis of void and bubble evolved after irradiation

Fig. 1. shows cross-sectional HAADF and BF STEM micrographs of the steels irradiated using 3.5-MeV Fe^{++} ions up to 480 dpa with 1 appm/dpa helium implantation. The darker and porous ion-damaged region is clearly distinguished from the bright and un-irradiated bulk region after the depth of 1,500 nm from the surface. A number of small-sized, but visually countable, black dots were observed along the ion path in the HAADF images. These black dots indicates the irradiation-induced voids and bubbles, arising mainly from the Z-contrast [6]. The quantitative cavity characterization was conducted over entire cavity-observed depth range from surface to ~1,000 nm; however, this region includes improper depth ranges having the neutron-atypical features: (i) outward Cr segregation and defect imbalance in near-surface region of <300 nm and (ii) injected interstitial effect
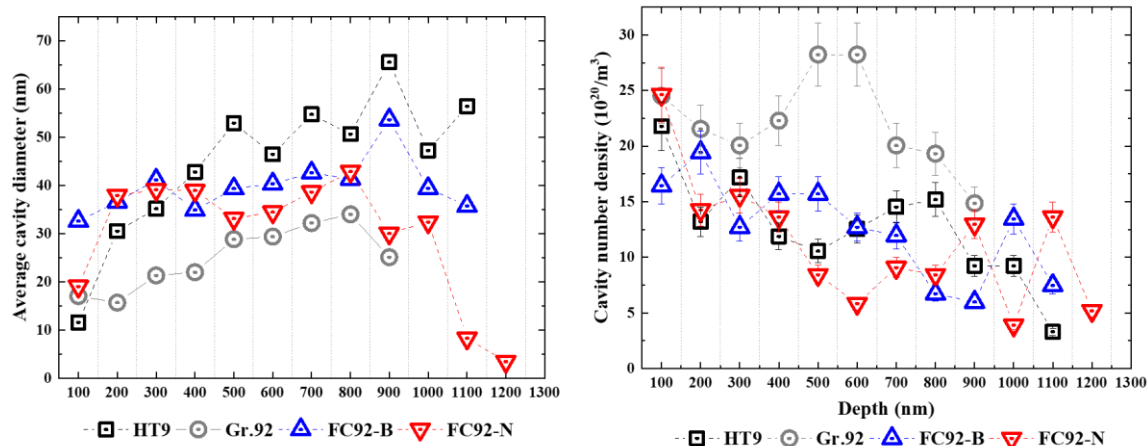
Fig. 2 Average cavity diameter and number density distribution in Fe^{++} ion-irradiated steels (radiation damage: 480 dpa) with He/dpa ratio of 1 appm/dpa.

at near-damage-peak region after 700 nm. Thus, a comparative assessment of swelling resistance between the tested alloys was made within a depth range of 400–700 nm.

Fig. 2. plots cavity diameter and number density distribution as a function of depth. All alloys exhibited similar trends in cavity size with an increasing depth. The size continuously increase from the surface to ~800–900 nm region and then stiffly dropped off. Average size of the examined cavities between 400–700 nm was measured 24.36 nm in HT9, 16.74 nm in Gr.92, 20.02 nm in FC92-B, and 18.01 nm in FC92-N, respectively. Although some fluctuations existed in the number density profiles, all steels showed similarities in their density distributions: it constantly decreased from the surface to the end-depth of cavity evolution except for Gr.92. For Gr.92, the density increased from the surface to its peak at 500–700 nm, followed by a stiff decrease as for the other alloys. Overall, the number density (10^{20}/m^3) in 400–700 nm depth region was measured as 12.55 for HT9, 26.50 for Gr.92, 13.71 for FC92-B, and 11.60 for FC92-N,

respectively. The highest population of voids and bubbles were observed in Gr.92 and the least was observed in FC92-N.

Swelling (Fig. 3.) over the entire-ion-damaged area reached 6.59% in HT9, 2.32% in Gr.92, 4.31% in FC92-B, and 2.12% in FC92-N; swelling between 400–700 nm was calculated as 8.99% in HT9, 2.94% in Gr.92, 5.44% in FC92-B, and 1.74% in FC92-N, respectively. The most swollen alloy was HT9 with a similar number density to that of FC92-B and approximately twice higher than that of FC92-N. But the alloy HT9 showed >5 nm larger average cavity size than other three alloys. This result indicates that the swelling resistances of the four tested alloys under given radiation damage condition strongly depend on not only the nucleation of a new void but also the growth of existing voids.

Swelling rate between 400–700 nm was obtained by assuming linear swelling within 400–700 nm region: 0.048%/dpa for HT9, 0.027%/dpa in Gr.92, 0.012%/dpa FC92-B, and 0.005%/dpa for FC92-N, respectively. These swelling rates are an order of magnitude less than the universal steady swelling rate of 0.2%/dpa postulated by Garner [7], indicating the four alloys still remained within the transient regime where the cavity nucleation and growth co-exist.

3.3. Elemental analysis on the irradiated alloys

Fig. 4. presents the panoramic HAADF images of irradiated steels with a magnification of 110k and corresponding EDS Fe/Cr/Ni/C/N mapping results. The EDS Cr/C/N maps demonstrates that Cr-rich rod-like precipitates containing C and N evolved only in FC92 series; however, two reference alloys only exhibited the $M_{23}C_6$ precipitates along the prior-austenite grain boundaries (PAGBs). A combination of their morphology and elemental ratio indicates that

Fig. 3 A depth-dependent swelling behaviors in Fe^{++} ion-irradiated steels (radiation damage: 480 dpa) with He/dpa ratio of 1 appm/dpa.
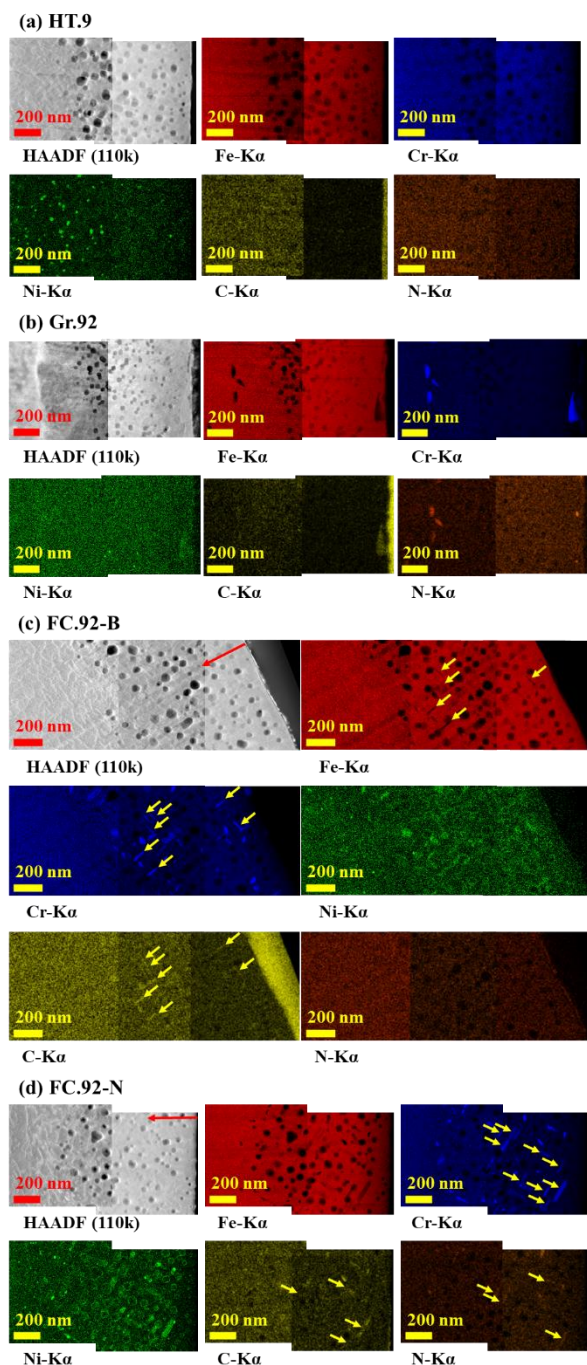
Fig. 4 HAADF images (magnification: 110k) and EDS elemental mapping results (Fe/Cr/Ni/C/N) of the Fe^{++} ion-irradiated steels (radiation damage: 480 dpa, pre-implanted He conc.: 0–480 appm varying with He/dpa ratio of 1 appm/dpa). The irradiation direction is marked with red arrows.

the thin needle-like precipitates in FC92 alloys correspond to M_2X, often reported in high-Cr F/M steels irradiated by neutrons [8–10] and/or ions [11–13]. The average size of M_2X was measured as 47.69 nm in FC92-B and 43.77 nm in FC92-N. In this study, any clear depth-/dpa-dependence in M_2X precipitation

was not found in average length, number density, and volume fraction for both of FC92 steels. This result may be attributed to elongated formation of M_2X along ion path.

One interesting result is that Cr and Ni atoms in all four alloys were redistributed as a result of radiation-induced segregation (RIS) behaviors. RIS-induced Ni shells at the periphery of the cavities and M_2X and G-phase precipitation evidence the alteration of chemical composition along the ion path. Before irradiation, Cr contents in each alloy were measured repeatedly on more than three different regions of ~10 μm^2 and averaged as 12.89 at% in HT9, 8.78 at% in Gr.92, 8.69 at% in FC92-B, and 8.52 at% in FC92-N, respectively.
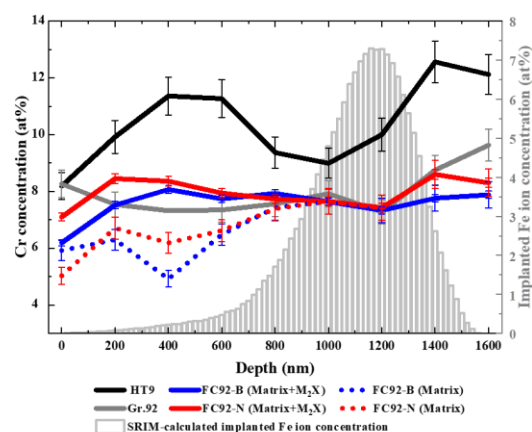
Fig. 5 Depth-dependent Cr concentration change along the ion path in the irradiated steels with a SRIM-calculated injected Fe ion concentration profile. The error bar in EDS elemental analysis reflects the relative error (2σ) with a 95% confidence level.

Fig. 5. shows a depth-dependent Cr depletion in irradiated alloys. For the near-surface region of <400 nm depth, all alloys exhibited lowered Cr contents compared to before-irradiation contents which increased to local maxima of 300–400 nm in HT9, 0–100 nm in Gr.92, 300–400 nm in FC92-B, and 200–300 nm in FC92-N, respectively. This result reflects the near-surface Cr-outward-segregation, which is commonly found in ion-irradiated Cr-containing F/M steels. It should be noted that Cr contents for both FC92 series in the 0–400 depth region differed depending on the presence of Cr-rich M_2X precipitates: for M_2X cases, Cr contents were measured as 6.19 at% at the surface and increased to 8.07 at% at 400 nm in FC92-B and 7.10 at% at the surface and increased to 8.36 at% at 400 nm in FC92-N. For cases without M_2X, Cr contents at the surface were 5.92 at% in FC92-B, and 5.03 at% in FC92-N, which are ~66% and ~55% of their nominal Cr contents, and 4.92 at% in FC92-B and 6.19 at% in FC92-N at 400 nm, respectively. After their local maxima of Cr contents in the first 400 nm region, Cr contents continuously decreased to their second local minima near the radiation damage peak by 3.5 MeV Fe^{++} ions. A lowered Cr contents in 400–

1400 nm region can be attributed to the accumulation of injected Fe^{++} ions in the vicinity of the Bragg's peak. This accumulation of Fe interstitial atoms near the Bragg's peak leads to the net increase in Fe atoms, lowering the relative abundance of other alloying elements. It should be noted that, as a result of M_2X precipitation, the Cr concentration in FC92 alloy matrix fell nearly half of their nominal contents. In the depth range outside the implanted Fe interstitial concentration peak, the Cr contents in all alloys recovered close to the nominal concentration levels and/or measured Cr contents from un-irradiated alloys.

This exceptional M_2X formation in FC92 alloys as well as the absence of M_2X in HT9 and Gr.92 can be attributed to B- and N-alloying in FC92 series. In other words, B-/N-addition may trigger the M_2X evolution in FC92 series after irradiation. B and N are one of the favored constituent elements for high-temperature application of F/M steels in fossil power generation [14,15]. The solute B in F/M steels is known to transforms the existing $M_{23}C_6$ into $M_{23}(C,B)_6$, thereby delaying the coarsening rate of $M_{23}C_6$ during long-term heat-treatment process [16], otherwise, the solute N promotes MX carbonitride, which is more thermally-stable than $M_{23}C_6$ at the elevated temperature [17]. Optimized balance between B and N contents was one of the priorities for developing FC92 steels having improved high-temperature creep resistance [18]. As a result, the FC92 series succeeded to exhibit an extremely low amount of $M_{23}C_6$ and a high degree of MX, while $M_{23}C_6$ was prevalent in the PAGBs in the two reference steels of HT9 and Gr.92 [5]. Earlier computational study by Getto demonstrates that the carbide precipitation during both heat treatment and ion irradiation in F/M steels, directly led to a decrease in solute C in the neighboring alloy matrix [19]. It should be avoided here to overstate the remaining solute C contents in neighboring alloy matrix because the qualitative elemental analysis on the trace elements, such as B, C, and N, was excluded due to the practical detection limit in point/areal EDS analysis. It is, however, still compelling to say that B- and N-addition in FC92 series led to a higher content of the remaining solute C in the matrix of FC92, and consequently, resulted in the exceptional M_2X evolution with the given irradiating condition.

3.4. Correlation between double-peak swelling and radiation-induced precipitation

One notable result is that the bimodal swelling curves were only found in FC92 series with radiation-induced M_2X precipitates; the unimodal swelling curves were found in the two reference steels with no (or little) M_2X precipitation behavior. This double-peak swelling behavior is one of the neutron-atypical features, often reported in ion-irradiated metals and alloys [20–22]. The origin and mechanism of the double-peak swelling in ion-irradiated steels have not been clearly understood yet, but recent studies showed that it is caused by defect imbalance along the ion path [20]. It should be noted that irradiating parameters, which affect the defect imbalance in the ion-irradiated alloys, were identically controlled for all of the four alloys. Thus, understanding this double-peak swelling behaviors in FC92 series requires another extrinsic factor. Cr is one of the favored ferrite-stabilizers in F/M steels, significantly involved in determining phase and precipitation behavior during long-term heat-treatment process [23]. Earlier studies of both neutron-/ion-irradiated steel alloys have shown that Cr has a strong effect on the swelling behavior by trapping defects [24,25]. Furthermore, soluble C also has a significant role in swelling, affecting defect clustering kinetics [26,27]. It can be concluded, thus, that RIP behaviors, especially M_2X evolution, in FC92 series may lead to Cr and C removal in the alloy matrix along ion path, and in turn, leave a low-alloyed near-surface region which is susceptible to cavity nucleation. This result has recently been published in the peer-reviewed journal, the *Journal of Nuclear Materials*, as experimental evidence that RIP can determine the swelling-depth profiles in irradiated alloys [5].

4. Conclusion

To test radiation resistance of FC92 steels, self-ion irradiation experiment was conducted on the four F/M steels of HT9, Gr.92, FC92-B, and FC92-N. The irradiation was performed to 480 dpa utilizing 3.5 MeV Fe^{++} ion at 475 °C with a helium pre-implantation of 1 appm/dpa. The post-irradiation microstructure characterization was performed with a focus on cavitational swelling using FE-TEM.

(1) Swelling observed in the alloys over the depth range of 400–700 nm reached the average value of 8.99% (HT9), 2.94% (Gr.92), 5.44% (FC92-B), and 1.74% (FC92-N). The most swelling-resistant alloy was FC92-N with a swelling rate of 0.005 %/dpa. These findings highlight a higher swelling resistance of FC92-N among the tested alloys.

(2) Radiation-induced M2X carbide evolved only in the FC92 series, but no clear depth-/dpa-dependence in M_2X precipitation was found in both FC92 alloys.

(3) As a result of the synergetic action of RIP-induced Cr removal and outward Cr sinking, Cr levels in the alloy matrix of FC92 series dropped to ~5 at% at the near-surface region, which is approximately half of the nominal concentration in 9Cr-FC92 series. This Cr depletion led to a locally low-alloyed region near the surface, which is susceptible to cavitational swelling. This result suggests that RIP-altered local chemical composition and consequent decrease in solute defect-trapping effects can lead to the *neutron-*

atypical swelling behavior of bimodal swelling profiles in the ion-irradiated steel alloys.

5. Acknowledgements

References

[1] G.S. Was, Challenges to the use of ion irradiation for emulating reactor irradiation, J. Mater. Res. 30 (2015) 1158.

[2] G.S. Was, Fundamentals of radiation materials science: metals and alloys, springer, 2016.

[3] R.L. Klueh, Elevated temperature ferritic and martensitic steels and their application to future nuclear reactors, Int. Mater. Rev. 50 (2005) 287–310.

[4] C.B. Lee, J.S. Cheon, S.H. Kim, J.-Y. Park, H.-K. Joo, Metal fuel development and verification for prototype generation IV sodium-cooled fast reactor, Nucl. Eng. Technol. 48 (2016) 1096–1108.

[5] M. Lee, G. Kim, Y. Jung, S. Ahn, Radiation-induced swelling and precipitation in Fe++ ion-irradiated ferritic/martensitic steels, J. Nucl. Mater. (2021) 153137.

[6] X. Wang, Q. Yan, G.S. Was, L. Wang, Void swelling in ferritic-martensitic steels under high dose ion irradiation: Exploring possible contributions to swelling resistance, Scr. Mater. 112 (2016) 9–14. https://doi.org/https://doi.org/10.1016/j.scriptamat.2015.08.032.

[7] F.A. Garner, M.B. Toloczko, B.H. Sencer, Comparison of swelling and irradiation creep behavior of fcc-austenitic and bcc-ferritic/martensitic alloys at high neutron exposure, J. Nucl. Mater. 276 (2000) 123–142. https://doi.org/https://doi.org/10.1016/S0022-3115(99)00225-1.

[8] P.J. Maziasz, Formation and stability of radiation-induced phases in neutron-irradiated austenitic and ferritic steels, J. Nucl. Mater. 169 (1989) 95–115. https://doi.org/https://doi.org/10.1016/0022-3115(89)90525-4.

[9] S.I. Porollo, A.M. Dvoriashin, Y.. Konobeev, F.A. Garner, Microstructure and mechanical properties of ferritic/martensitic steel EP-823 after neutron irradiation to high doses in BOR-60, J. Nucl. Mater. 329–333 (2004) 314–318. https://doi.org/https://doi.org/10.1016/j.jnucmat.2004.04.310.

[10] A.M. Dvoriashin, S.I. Porollo, Y.. Konobeev, F.A. Garner, Influence of high dose neutron irradiation on microstructure of EP-450 ferritic–martensitic steel irradiated in three Russian fast reactors, J. Nucl. Mater. 329–333 (2004) 319–323. https://doi.org/https://doi.org/10.1016/j.jnucmat.2004.04.309.

[11] L. Shao, X. Lu, X. Wang, I. Rusakova, J. Liu, W.-K. Chu, Retardation of boron diffusion in silicon by defect engineering, Appl. Phys. Lett. 78 (2001) 2321–2323.

[12] E. Getto, K. Sun, G.S. Was, Characterization of M2X formed during 5 MeV Fe2+ irradiation, J. Nucl. Mater. 485 (2017) 154–158. https://doi.org/https://doi.org/10.1016/j.jnucmat.2016.12.027.

[13] H. Cheng, W. Song, Y. Shen, X. Huang, Z. Xu, Q. Li, Z. Shang, Z. Yang, Fe13+ ion irradiation-induced M2X precipitate in P92 steel at 700°C up to 1.62 dpa, J. Nucl. Mater. 498 (2018) 314–320. https://doi.org/https://doi.org/10.1016/j.jnucmat.2017.09.035.

[14] F. Abe, T.-U. Kern, R. Viswanathan, Creep-resistant steels, Elsevier, 2008.

[15] F. Abe, Precipitate design for creep strengthening of 9% Cr tempered martensitic steel for ultra-supercritical power plants, Sci. Technol. Adv. Mater. 9 (2008) 13002.

[16] F. Abe, Effect of boron on microstructure and creep strength of advanced ferritic power plant steels, Procedia Eng. 10 (2011) 94–99.

[17] K. Sawada, K. Kubo, F. Abe, Contribution of coarsening of MX carbonitrides to creep strength degradation in high chromium ferritic steel, Mater. Sci. Technol. 19 (2003) 732–738.

[18] V.C. Igwemezie, C.C. Ugwuegbu, U. Mark, Physical metallurgy of modern creep-resistant steel for steam power plants: microstructure and phase transformations, J. Metall. 2016 (2016).

[19] E. Getto, G. Vancoevering, G.S. Was, The co-evolution of microstructure features in self-ion irradiated HT9 at very high damage levels, J. Nucl. Mater. 484 (2017) 193–208. https://doi.org/https://doi.org/10.1016/j.jnucmat.2016.12.006.

[20] L. Shao, C.-C. Wei, J. Gigax, A. Aitkaliyeva, D. Chen, B.H. Sencer, F.A. Garner, Effect of defect imbalance on void swelling distributions produced in pure iron irradiated with 3.5 MeV self-ions, J. Nucl. Mater. 453 (2014) 176–181.

[21] E. Getto, Z. Jiao, A.M. Monterrosa, K. Sun, G.S. Was, Effect of pre-implanted helium on void swelling evolution in self-ion irradiated HT9, J. Nucl. Mater. 462 (2015) 458–469.

[22] T. Aruga, Y. Katano, K. Shiraishi, Double

peak of voidage depth profile in carbon or nitrogen ion irradiated 316 stainless steel, J. Nucl. Mater. 122 (1984) 191–195. https://doi.org/https://doi.org/10.1016/0022-3115(84)90594-4.

[23] R.L. Klueh, D.R. Harries, High-chromium ferritic and martensitic steels for nuclear applications, in: AsTM West Conshohocken, PA, 2001.

[24] E.A. Little, Void-swelling in irons and ferritic steels: I. Mechanisms of swelling suppression, J. Nucl. Mater. 87 (1979) 11–24.

[25] S.I. Porollo, A.M. Dvoriashin, A.N. Vorobyev, Y.. Konobeev, The microstructure and tensile properties of Fe–Cr alloys after neutron irradiation at 400°C to 5.5–7.1 dpa, J. Nucl. Mater. 256 (1998) 247–253. https://doi.org/https://doi.org/10.1016/S0022-3115(98)00043-9.

[26] Y.V. Konobeev, A.M. Dvoriashin, S.I. Porollo, F.A. Garner, Swelling and microstructure of pure Fe and Fe–Cr alloys after neutron irradiation to ~26dpa at 400°C, J. Nucl. Mater. 355 (2006) 124–130. https://doi.org/https://doi.org/10.1016/j.jnucmat.2006.04.011.

[27] D.S. Gelles, Fusion Reactor Materials, Semiannual Progress Report for the Period Ending March 31, 1994, DOE/ER-0313/16, Oak Ridge National Laboratory, Oak Ridge, Tennessee, 1994.